Journal of Applied Fluid Mechanics, Vol. 17, No. 1, pp. 136-147, 2024.
Available online at www.jafmonline.net, ISSN 1735-3572, EISSN 1735-3645.
https://doi.org/10.47176/jafm.17.1.2122

Investigation of An Inverted Bow on Frigate Hull Resistance

S. Samuel[1†], A. Wicaksono[1], W. A. Kurniawan[1], E. S. Hadi[1], T. Tuswan[1], A. Trimulyono[1] and M. Muryadin[2]

[1] *Department of Naval Architecture, Faculty of Engineering, Diponegoro University, Semarang, 50275, Indonesia*
[2] *Research Center for Hydrodynamics Technology, National Research and Innovation Agency (BRIN), Surabaya 60117, Indonesia*

†*Corresponding Author Email: samuel@ft.undip.ac.id*

ABSTRACT

This study discusses the inverted bow design on the combatant hull form. Changes in the shape of the stem angle and flare bow are used as analytical parameters to investigate the ship's performance. Ship resistance and motion will be predicted using the Computational Fluid Dynamics (CFD) approach using the Reynolds Averaged Navier Stokes (RANS) equation and the k-ε turbulence model. The volume of fluid (VOF) method is applied to simulate the change in the free surface between water and air using an overset mesh technique. The ship's movement is limited to sinkage and trim motions, so the movement's accuracy can be predicted. The results revealed that the inverted bow reduced the total resistance by 6.30%, whereas the trim and sinkage showed no significant changes. The breakdown of the reduction ratio showed that friction resistance components were reduced by 10.62%, wave resistance by 44.05%, and viscous-pressure resistance by 45.33%. This highlights the effectiveness of an inverted bow in optimizing wave and viscous pressure, enhancing overall ship performance.

Article History

Received June 24, 2023
Revised September 5, 2023
Accepted September 8, 2023
Available online November 1, 2023

Keywords:

Inverted bow
Resistance
Sinkage
Trim
Computational fluid dynamics

1. INTRODUCTION

Greenhouse Gas (GHG) emissions carry unforeseen risks to the natural ecosystem. One of the most significant emitters is the maritime sector. According to the International Maritime Organization / IMO (2020), ship emissions accounted for around 2.89% of global CO2 emissions and are expected to increase by 90-130% in 2050. In response to this matter, IMO (2021) has implemented various measures, including the Energy Efficiency Design Index (EEDI), the Energy Efficiency Existing Ship Index (EEXI), the Ship Energy Efficiency Management Plan (SEEMP), the Carbon Intensity Indicator (CII), and other initiatives. Some regulations require that every ship built after January 1, 2013, be certified using EEDI. Most new ships will need to be 10% more efficient starting in 2015, 20% more efficient by 2020, and 40% more efficient by 2030 as a result of this requirement (Wiliyan et al., 2023). That may be connected to ship resistance, one of the critical variables employed in calculations that enable researchers to work more effectively and optimally shapely build ships. Several studies have been implemented to reduce the ship's total resistance, including the frictional resistance well done by Yanuar et al. (2012) using bubble drag reduction. In addition, pressure resistance and wave resistance can be optimized by changing the shape of the bow (Lee et al., 2017) and hull (Liu et al., 2021).

The inverted bow possesses unique characteristics that set it apart from conventional designs in general. Its distinct features include the design of the flare and stem angle. The research on the inverted bow was initially conducted on a combatant hull-type ship (FFG-7) by White et al. (2016), which demonstrated a decrease in resistance with the implementation of the inverted bow. Additionally, it was observed that in regular waves, the inverted bow functions like a spring, increasing the amplitude of motion while reducing acceleration. The interaction between the inverted bow and irregular waves showed improved seakeeping performance. Experimental results indicated that the inverted bow reduced trimming motion by up to 15.9% in Sea State 5. Talukdar (2022) also conducted similar research on frigates, finding that the inverted bow reduced wave resistance by 8.1% and total resistance (RT) by 6.8% at maximum speed. Keuning et al. (2006), in their study on the behavior of fast patrol boats with the inverted bow concept, likened it to a damped spring-mass system, softening the spring constant of the system for vertical motion. This led to increased trim and sinkage movements while reducing vertical acceleration.

Advancements in computing technology have enabled researchers to conduct numerical research, which is more efficient and accessible than experimental testing. This method allows for the simulation and validation of all types of problems in real-life situations using experimental data. The Computational Fluid Dynamics (CFD) method offers several approaches for solving fluid flow problems, such as Reynolds Average Navier-Stokes (RANS), Large Eddy Simulation (LES), and Direct Numerical Solution (DNS). However, LES and DNS require more computational memory for calculations (Ozdemir et al., 2014; Hoa et al., 2019). Consequently, RANS is widely used in the shipping industry as a practical solution. Previous CFD studies utilizing the RANS method have been conducted on various aspects of resistance analysis. These include investigations into turbulent free surface flow on fast-displacement ships (Ozdemir et al., 2014), the influence of water depth on ship resistance (Hoa et al., 2019), the impact of new types of bow appendages on ship resistance (Liu et al., 2020), prediction of wave resistance at high Froude numbers (Kinaci et al., 2016), predict discharge (flow rate) in compound channels (Kulkarni & Hinge, 2021a, b; 2023), the effect of trim configuration on ship resistance (Le et al., 2021), and benchmark studies of the FINETM/Marine code for ship resistance calculations (Firdhaus et al., 2021). These studies have yielded promising results in utilizing the RANS method.

This study aims to reduce the resistance of ships by modifying the bow shape with an inverted bow. Additionally, the study will observe the trim and sinkage movements resulting from the ship's speed response under calm water conditions. This research is valuable for ship designers to ensure compliance with the regulations set by the IMO. The advancement of computing technology enables researchers to predict ship resistance and dynamic motion. The novelty of this study lies in conducting a numerical investigation of the inverted bow. Previous studies by White et al. (2016) focused solely on seakeeping analysis, while Talukdar (2022) examined variations of a reverse bow.

In contrast, this research presents a novel approach by developing a modified stem angle and flare bow design. The numerical simulation will be compared with the study conducted by Ozdemir et al. (2014). The discussion will encompass various aspects of ship performance, including resistance and motion, with a particular emphasis on trim and sinkage. Ship resistance components comprise frictional resistance, viscous pressure resistance, and wave-making resistance. Frictional resistance arises from the interaction between the ship's hull surface and the surrounding fluid, accounting for a large proportion of total resistance at low speeds. Wave-making resistance originates from disturbances created by the ship's movement through the water and air interface, increasing significantly with higher navigation speeds. In high-speed displacement ships, this component represents more than 50% of the total resistance reduction (Liu et al., 2020). Consequently, reducing wave-making resistance becomes crucial to minimizing overall ship resistance and is achievable through optimization of bow design to attain an optimal form.

2. METHODOLOGY

2.1 Object of Research

The object used in this research is a navy combatant frigate which is simulated in calm water conditions. The ship data is a scale model that has been tested experimentally and numerically by Ozdemir et al. (2014). The CFD model uses a 1:36 scale with details of the main sizes in Table 1.

Figure 1 shows the 2-D barehull model used in this research. Modification of the inverted bow will be carried out on this model as much as possible not to change the main size details of the ship.

2.2 Research Parameters

This research is focused on the effect of the inverted bow on the frigate. Fixed parameters are the length of the waterline, displacement, breadth, and draft. While the parameter variables are ship speed, stem angle, and flared bow.

Table 1 Model ship particulars

Main size	Unit	Full scale 1:1	Model scale 1:36
Length of waterline (LWL)	m	139.07	3.866
Breadth (B)	m	18.20	0.508
Height (H)	m	11.20	0.31
Draft (T)	m	5.05	0.14
Displacement (Δ)	Ton	5768.24	0.124
Block coefficient (C_B)	-	0.489	0.487
Wetted surface area (WSA)	m^2	2550.30	1.883

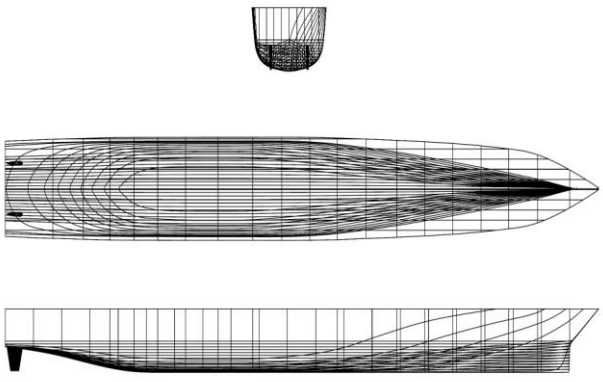

Fig. 1 Lines plan barehull

The angle of inclination on the longitudinal profile of the ship's bow tip, as seen in Fig. 2, is referred to as the stem angle. The flared bow is the angle in the transverse section measured from the high line and water line junction, as shown in Fig. 3, and positioned 0.08 m from the FP point, as shown in Fig. 2 (Kiryanto et al., 2019).

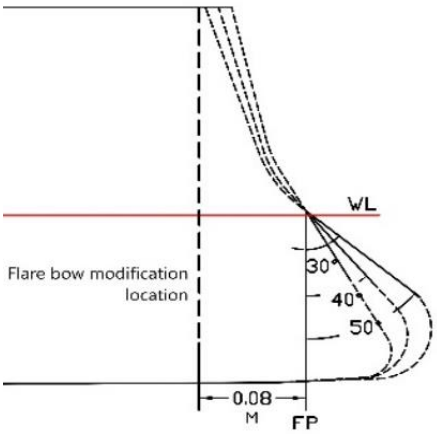

Fig. 2 Stem angle (30°, 40°, 50°)

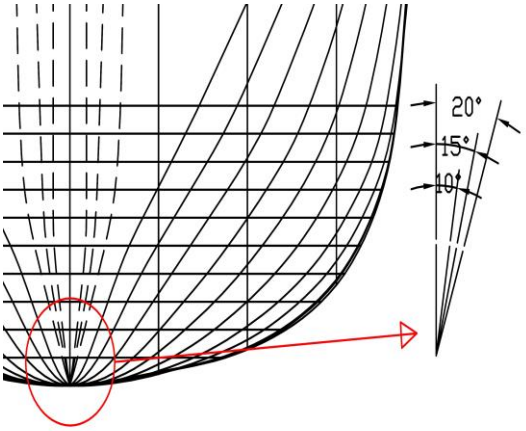

Fig. 3 Flare bow (10°, 15°, 20°)

2.3 Model Variations

The 3D model is created using the Non-Uniform Rational B-spline Surface (NURBS), a mathematical model utilized in computer graphics. The modeling process involves defining lines and surfaces, while the polysurface technique is employed to generate solid shapes. This research analyzed nine variations of the inverted bow model and one original model with detailed changes in Table 2.

Table 2 Model variations and volume correction

Model	Stem angle	Flare bow	Volume (m^3)	Volume difference (%)
Barehull	-	-	0.40513	-
IB3010	30°	10°	0.40476	-0.091
IB3015	30°	15°	0.40512	-0.002
IB3020	30°	20°	0.40632	-0.294
IB4010	40°	10°	0.40475	-0.094
IB4015	40°	15°	0.40511	-0.005
IB4020	40°	20°	0.40631	-0.291
IB5010	50°	10°	0.40474	-0.096
IB5015	50°	15°	0.40511	-0.005
IB5020	50°	20°	0.40632	-0.294

Fig. 4 Side view 3D model for barehull and inverted bow

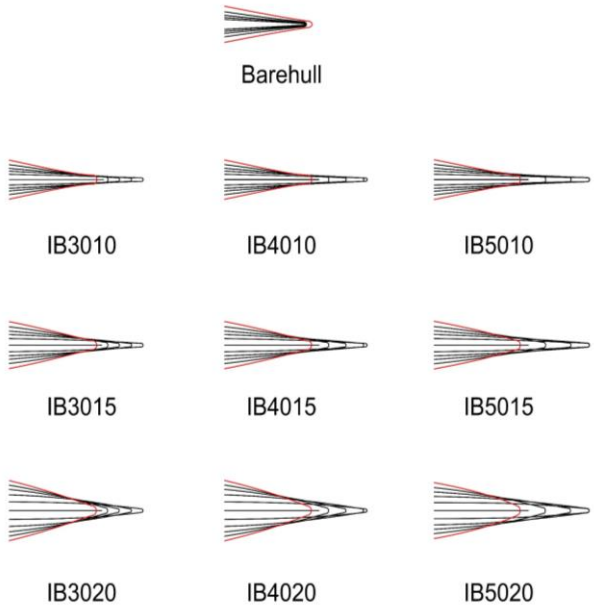

Fig. 5 Waterline view at bow area from model variations

As depicted in Fig. 4, the inverted bow model exhibits an increase in volume above the main deck. This addition aims to equalize the overall volume of the ship between the original and inverted bow models while also reducing deck wetness (White et al., 2016). Figure 5 displays the waterline cut to shape the ship's bow area from a top view for each variation. The waterline cut is taken at a draft range of 0.028 to 0.14 m, with the maximum draft indicated by the red line.

2.4 Numerical Approach

Using the computational fluid dynamics (CFD) approach, the ship model is simulated in this work. The unsteady Reynolds-Averaged Navier-Stokes equations, a method of problem-solving based on the principle of conservation of mass and momentum, are used to complete the hydrodynamic simulation (Kinaci et al., 2016). Below are the URANS equation.

$$\frac{\partial U_i}{\partial x_i} = 0 \tag{1}$$

$$\frac{\partial U_i}{\partial t} + \frac{\partial (U_i U_j)}{\partial x_j} = -\frac{1}{\rho}\frac{\partial P}{\partial x_i} + \frac{\partial}{\partial x_i}\left(2\nu S_{ij} - \overline{u_i' u_j'}\right) \tag{2}$$

Where U_i and u_i' express the mean and fluctuation velocity component in the direction of the Cartesian coordinate x_i, P is the mean pressure, ρ is the density, ν is the molecular kinematic viscosity and S_{ij} is the mean strain-rate tensor. The strain-rate tensor is defined as

$$S_{ij} = \frac{1}{2}\left(\frac{\partial U_i}{\partial x_j} + \frac{\partial U_j}{\partial x_i}\right) \tag{3}$$

The last term on the right-hand side of Eq. (2) is denoted as the Reynolds stress tensor which is given by

$$\tau_{ij} = \overline{u_i' u_j'} = \mu_t \left(\frac{\partial U_i}{\partial x_j} + \frac{\partial U_j}{\partial x_i} - \frac{1}{3}\frac{\partial U_k}{\partial x_k}\partial_{ij}\right) - \frac{2}{3}\rho k \partial_{ij} \tag{4}$$

The Boussinesq (eddy-viscosity) hypothesis obtained with the $k-\varepsilon$ turbulence model is expressed by

$$\mu_t = \frac{1}{2}\frac{\rho \tau_{ij}}{S_{ij}} \tag{5}$$

The k-ε turbulence model specifies that the turbulent eddy viscosity is calculated by

$$\mu_t = c_\mu \rho \frac{k^2}{\varepsilon} \tag{6}$$

The turbulent kinetic energy k and the rate of dissipation of the turbulent energy ε are calculated below

$$\frac{\partial \rho k}{\partial t} + \frac{\partial \rho U_j k}{\partial x_j} = \frac{\partial}{\partial x_j} + \left[\left(\mu + \frac{\mu_t}{\sigma_t}\right)\frac{\partial k}{\partial x_j}\right] + P_k - \rho\varepsilon \tag{7}$$

$$\frac{\partial \rho \varepsilon}{\partial t} + \frac{\partial \rho U_j \varepsilon}{\partial x_j} = \frac{\partial}{\partial x_j} + \left[\left(\mu + \frac{\mu_t}{\sigma_\varepsilon}\right)\frac{\partial \varepsilon}{\partial x_j}\right] + \frac{\varepsilon}{k}(c_{\varepsilon 1} P_k - c_{\varepsilon 2}\rho\varepsilon) \tag{8}$$

When the energy dissipation rate ε and the kinetic energy k are combined, the turbulent viscosity μ_t may be determined. A near-wall function uses a realizable k-ε two-layer turbulence technique to describe the velocity profile near the wall (Mohan & Pattamatta, 2015). The following calculation bases the time-step on the ITTC guideline (ITTC, 2011).

$$\Delta t\ ITTC = 0.005 \sim 0.01\ \frac{L}{V} \tag{9}$$

As shown in Fig. 6, the time-step value is between 0.0075 and 0.009. The time-step determination of the CFD calculation depends on the ship's speed. The faster the ship's speed, the smaller the time-step used. Based on the calculation recommended by ITTC in Eq. (9), ship length is noted as L and ship speed notes as V. The wall distance (Y+) is used in the area affected by the viscosity effect between the wall and the turbulent region. Y+ is defined as the non-dimensional distance of the first grid node from the wall surface, normalized by the local viscous length scale. In previous studies, the Y+ value ranged from 45 to 110 (Ozdemir et al., 2014). Meanwhile, ITTC (2011)

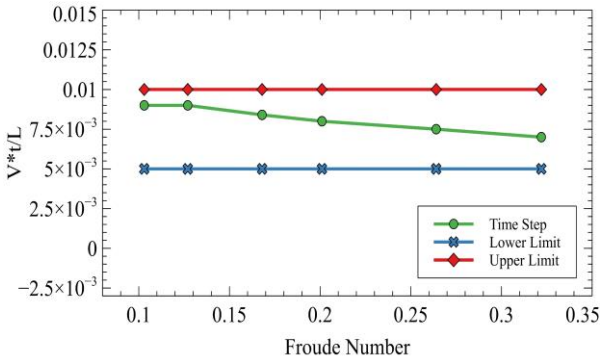

Fig. 6 Illustration of time-step

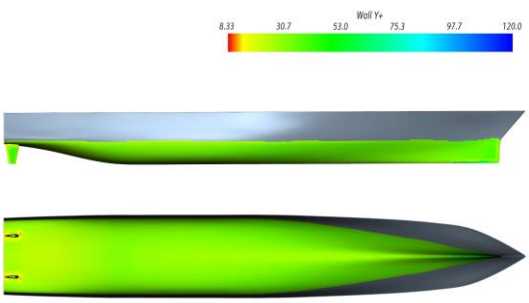

Fig. 7 Wall Y+ barehull for Fn = 0.201

recommends that the Y+ value is 30 < Y+ < 100. It is calculated using the following formula

$$Y^+ = \frac{(\rho \,.\, U \,.\, y)}{\mu} \tag{10}$$

Where U is the friction velocity at the wall, y is the distance from the wall to the first grid node, and μ is the dynamic viscosity of the fluid.

The average Y+ value on the ship is between 45 and 65, as seen in Fig. 7. According to (ITTC, 2011; Firdhaus et al., 2021), the Volume of Fluid (VOF) approach replicates the free surface change at the water/air interface. The water utilized had a density and viscosity of 998.9 kg/m^3 and 1.1088 x 10^{-4} Pa-s, respectively.

2.5 Ship Resistance Computation

The total resistance obtained from the analysis was simulated utilizing Simcenter Star-CCM+ CFD Code based on the RANS approach. The resistance output is divided into two components, which can be expressed using the following formulas

$$R_T = R_F + R_P \quad \text{(CFD output)} \tag{11}$$

$$C_T = C_F + C_P \quad \text{(non-dimensional unit)} \tag{12}$$

C_T denotes the total resistance coefficient, while C_F and C_P are frictional resistance coefficient and pressure resistance coefficient. In this study, the coefficients are formulated in the following manner

$$C_x = R_x \,/\, 0.5 \,.\, \rho \,.\, WSA \,.\, Vs^2 \tag{13}$$

Where x may refer to any resistance component used in that equation, WSA is the wetted surface area, and Vs is

the ship's speed. Furthermore, the pressure resistance coefficient can be broken down into components of the wave-making resistance coefficient (C_W) and viscous-pressure resistance coefficient (C_{VP}) (Lewis, 1998; Fitriadhy et al., 2020).

$$C_P = C_W + C_{VP} \tag{14}$$

To obtain C_W and C_{VP}, we need to determined the form factor $(1 + K)$ which is derived from the following equation.

$$1 + K = \lim_{Fn \to 0} \frac{C_T}{C_F} \tag{15}$$

The form factor approach assumes that viscous resistance has a similar proportion to frictional resistance for a flat plate at an equal Reynolds number. Hence, the resistance tests are performed at low Froude number (Fn = 0.103), where wave resistance is considered negligible (Ozdemir et al., 2014). After obtaining the form factor, we can determine C_W and C_{VP} using the following equations.

$$C_W = C_T - (1 + K)\, C_F \tag{16}$$

$$C_{VP} = K\, C_F \tag{17}$$

$$R_T = R_F + R_W + R_{VP} \tag{18}$$

After acquiring the coefficients for each resistance component, they can be substituted into Eq. (13) to calculate the resistance of each component. As a result, the final total resistance will be the sum of the three resistance components, as shown in Eq. (18).

2.6 Meshing Strategy

This study uses a trimmed structured mesh with an anisotropic mesh method and focuses on the x, y, and z coordinates. The domain size and boundary conditions refer to the ITTC recommendation (ITTC, 2011). The details of the domain size are shown in Table 3, while the boundary conditions are shown in Table 4.

Figure 8 illustrates a virtual towing tank, where Lpp is the Length between perpendiculars, B is the ship's breadth, and H is the boat's height. As shown in Fig. 9, if the backdrop comprises receptor cells and the overset comprises acceptor cells, the mesh overset approach separates the domain into two sections (Samuel et al,. 2021a, b).

Table 3 Domain dimensions

Parameter	Background	Overset
Length (M)	2.5 Lpp from FP	0.3 from AP
	2.5 Lpp from AP	0.3 from FP
Height (M)	1.5 Lpp from the deck	1.0 H from the deck
	1.5 Lpp from the keel	1.0 H from the keel
Wide (M)	2.0 Lpp from symmetry	1.0 B from symmetry

Table 4 Boundary conditions

Surface Area	Background	Overset
Top	Velocity inlet	Overset mesh
Bottom	Velocity inlet	Overset mesh
Inlet	Velocity inlet	Overset mesh
Outlet	Pressure outlet	Overset mesh
Back	Velocity inlet	Overset mesh
Symmetry	Symmetry plane	Symmetry plane
Hull	-	No slip wall

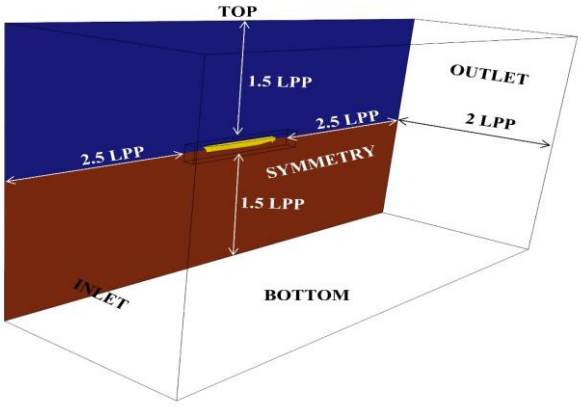

Fig. 8 Illustration of virtual towing tank

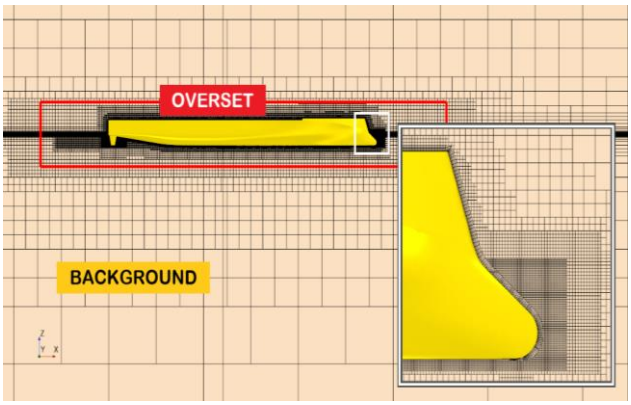

Fig. 9 Background, overset, and the bow section

To minimize the inaccuracy of the results, it is crucial to do an independent mesh and compare it with experimental data. This ensures that the analysis results stay the same as the mesh density increases (Fathuddiin & Samuel, 2021). In this simulation, five conditions of mesh density and full mesh were obtained, which can be seen in Tables 5 and 6.

Table 5 Total mesh

Grid no.	Mesh quality	Total mesh
1	Very coarse	779556
2	Coarse	1227205
3	Medium	1755342
4	Fine	2233457
5	Very fine	2519969

Table 6 Mesh density

Part name	Very coarse	Coarse	Medium	Fine	Very fine
Bow	0.0020 Lpp	0.0016 Lpp	0.0014 Lpp	0.0013 Lpp	0.0012 Lpp
Stern	0.0020 Lpp	0.0016 Lpp	0.0014 Lpp	0.0013 Lpp	0.0012 Lpp
Free surface	0.0078 Lpp	0.0065 Lpp	0.0057 Lpp	0.0052 Lpp	0.0049 Lpp
Near ship	0.0078 Lpp	0.0065 Lpp	0.0057 Lpp	0.0052 Lpp	0.0049 Lpp
Hull	0.0039 Lpp	0.0032 Lpp	0.0025 Lpp	0.0025 Lpp	0.0025 Lpp

3. RESULT AND DISCUSSION

3.1 Mesh Independence and Validation

The mesh size has an important influence on the computational calculation procedure. Because of the many elements, a good mesh gives more accurate results but takes a long time. Therefore, an independent mesh is needed to get the correct number of features with stable/dependent results (Fathuddiin & Samuel, 2021).

In Fig. 10, the simulation compares the resistance, trim, and sinkage values to the number of elements. The results show that the calculated data becomes more convergent as the number of meshes increases. The red-dotted line shows the limit of convergence. The results of grid #3, grid #4, and grid #5 indicate the stability of the value. Compared to grids #4 and #5, which require a longer simulation time, the CFD simulation was run using grid #3 with a full mesh of 1.75M.

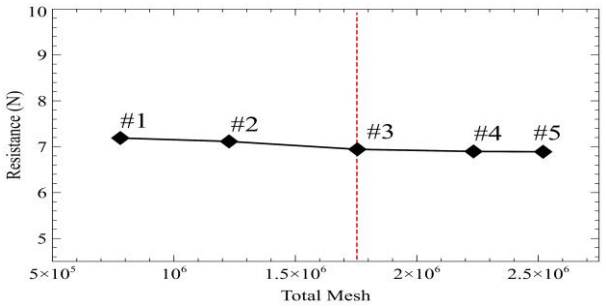

(a) Resistance

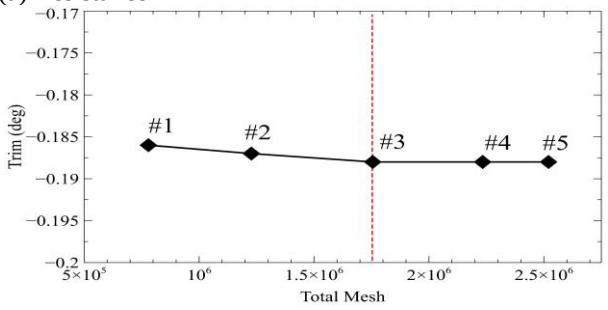

(b) Trim

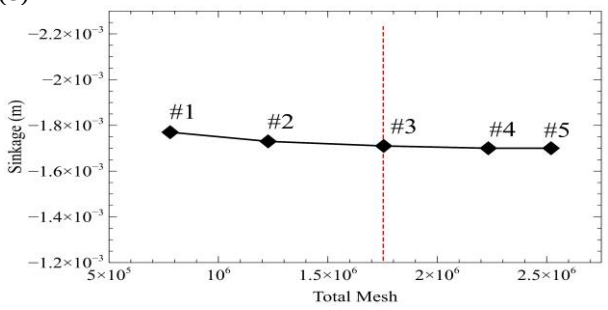

(c) Sinkage

Fig. 10 Mesh independency for resistance (a), trim (b), and sinkage (c) at Fn = 0.201

Figure 11 shows the computational results of the barehull model at Fn = 0.201. The plot results show that all data converges at a physical time of 10s. After deciding on the mesh size, the CFD model is validated by comparing the overall resistance value and coefficient with the experimental data. The total resistance of the ship is shown in Eq. (11).

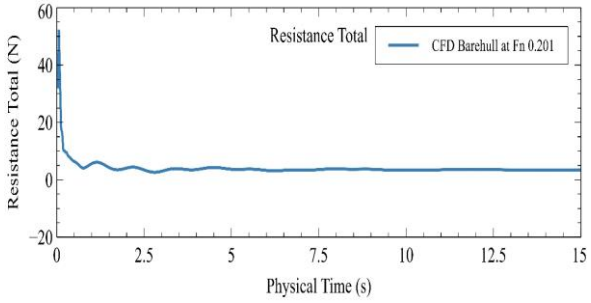

(a) Resistance

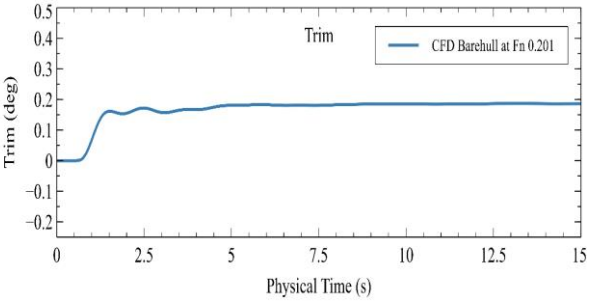

(b) Trim

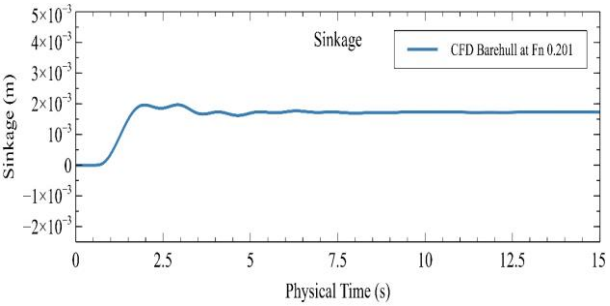

(c) Sinkage

Fig. 11 CFD convergence data samples for total resistance (a), trim (b), and sinkage (c) on barehull model at Fn 0.201

Table 7 Model validatio

Fn	V (m/s)	Experiment (Ozdemir et al., 2014)		CFD		Difference (%)
		R_T (N)	$C_T x(10^{-3})$	R_T (N)	$C_T x(10^{-3})$	
0.103	0.634	1.988	4.928	1.970	4.884	0.89
0.127	0.784	2.947	4.773	2.907	4.709	1.35
0.168	1.037	4.902	4.540	4.947	4.582	0.92
0.201	1.239	6.874`	4.461	6.943	4.506	1.01
0.264	1.628	12.245	4.597	12.608	4.733	2.96
0.322	1.980	19.650	4.982	19.674	4.988	0.12

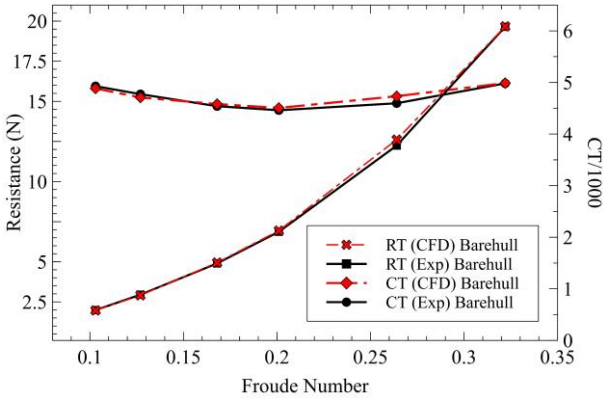

Fig. 12 Comparison of total resistance and total resistance coefficient between CFD and Experiment

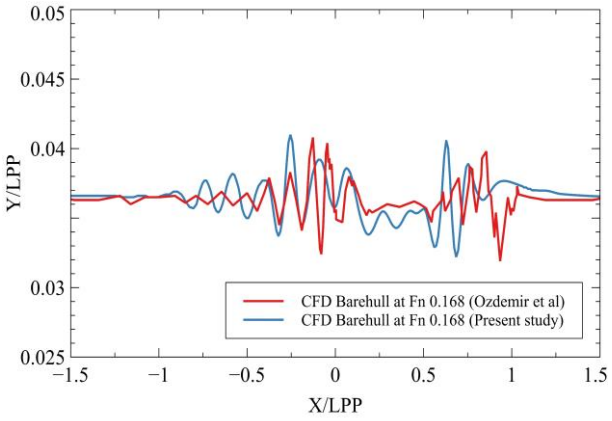

Fig. 13 Comparison of barehull surface elevation at Fn 0.168 with previous research

The following is the result of the comparison of the total resistance of the boat and the coefficient of the ship's resistance, where the calculation is based on six-speed conditions, as shown in Table 7

Figure 12 compares the total resistance and the coefficient of total resistance between the CFD model and experimental data. Table 7 shows that the total resistance at Fn 0.103 and Fn 0.127 has a smaller value of 0.89% and 1.35% from the experiment. While at Fn 0.168 to Fn 0.322, the value is greater than the experiment by 0.12% - 2.96%. The differences between CFD and experiments can occur because fluid phenomena are difficult to predict without errors. This study can be seen in previous studies (Samuel et al., 2019, 2022).

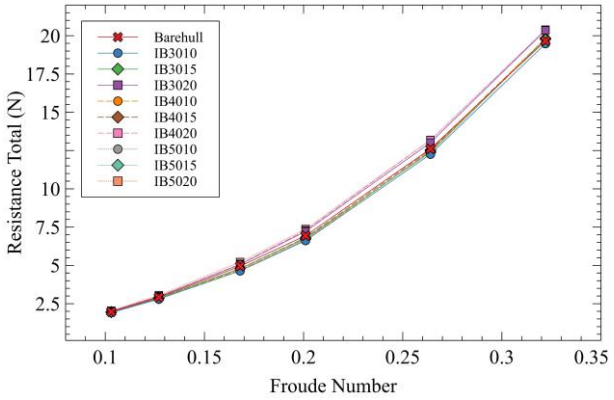

Fig. 14 Inverted bow total resistance (R_T) analysis resul

Table 8 Total resistance reduction

Model	Fn 0.201		Fn 0.264	
	R_T (N)	Reduction (%)	R_T (N)	Reduction (%)
Barehull	6.943	-	12.608	-
IB3010	6.619	4.66	12.259	2.77
IB3015	6.766	2.55	12.376	1.84
IB4010	6.641	4.36	12.434	1.38
IB4015	6.810	1.92	12.544	0.51
IB5010	6.664	4.03	12.476	1.05
IB5015	6.716	3.28	12.460	1.17

Figure 13 shows the comparison of surface elevation to the previous CFD studies. Simulation is taken on Fn = 0.168 barehull model. There are some differences between the current results and the results of previous researchers, which could be due to differences in the mesh and the numerical approach used.

3.2 Analysis Results on Inverted Bow

The total resistance of the ship consists of the sum of frictional resistance (R_F), wave-making resistance (R_W), and viscous-pressure resistance (R_{VP}). The analysis results of each resistance component are shown in the following figure.

The optimal ship speed is at Fn 0.201 and Fn 0.264. After the application of an inverted bow, there is a reduction in total resistance. Table 8 shows that the IB3010 model has the optimum reduction at these two speeds. At Fn 0.201, it decreased by 4.66%, and at Fn

Table 9 Total resistance reduction at Fn 0.168

Model	Fn 0.168	
	R_T (N)	Reduction (%)
Barehull	4.947	-
IB3010	4.636	6.30
IB3015	4.789	3.19
IB4010	4.696	5.08
IB4015	4.795	3.08
IB5010	4.744	4.10
IB5015	4.795	2.82

Table 10 Ratio reduction of resistance component at Fn 0.168

	Barehull	IB 3010	Difference (N)	Proportion (%)
R_T (N)	4.947	4.636	0.311	100
R_F (N)	3.586	3.553	0.033	10.62
R_W (N)	0.572	0.435	0.137	44.05
R_{VP} (N)	0.789	0.648	0.141	45.33

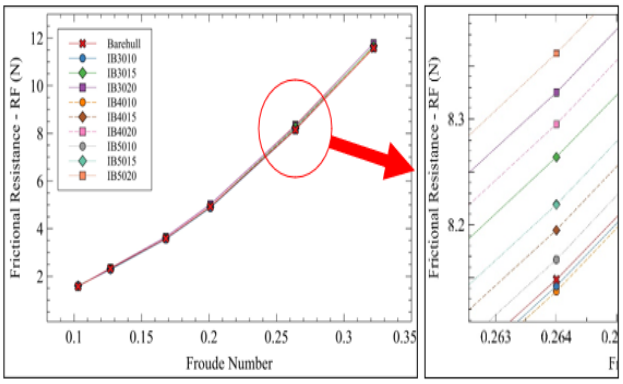

Fig. 15 Inverted bow frictional resistance (R_F) analysis result

0.264, it decreased by 2.77%. However, when viewed as a whole simulation, the most significant reduction in total resistance occurs at IB3010 Fn 0.168 with a value of 6.30%, where the proportion of all resistance components is listed in the following table.

Furthermore, Table 10 illustrates the proportions of each resistance component. These proportions are derived from the largest reduction in total resistance observed at Fn 0.168 as shown in Table 9. The analysis of the reduction ratio showed that frictional resistance components decreased by 10.62%, wave resistance by 44.05%, and viscous-pressure resistance by 45.33%.

The friction resistance (RF) component is shown in Fig. 15. The analysis result shows that its value has not changed significantly. However, when explicitly viewed, the most significant increase occurred in IB5020 Fn 0.264 with a value of 2.62%. While in the overall simulation, the frictional resistance increased from 0.01% to 2.62%.

Based on Fig. 16, it can be seen that the wave resistance does not change significantly at the speed of Fn 0.103 and Fn 0.127 because low-speed waves have yet to form. Differences begin to form at Fn 0.168 and above. With an inverted bow, wave resistance has been reduced. The highest reduction occurred in IB5015 Fn 0.264, shown in Table 11, with a value difference of 0.255 N or 9.55% from the barehull model.

Figure 17 is the result of viscous-pressure resistance. It was found that the optimal reduction was at Fn 0.322. As shown in Table 12, the most significant decrease occurred in IB3010, with a value of 17.06%. In comparison, the highest increase was in IB5020, with a value of 21.36%.

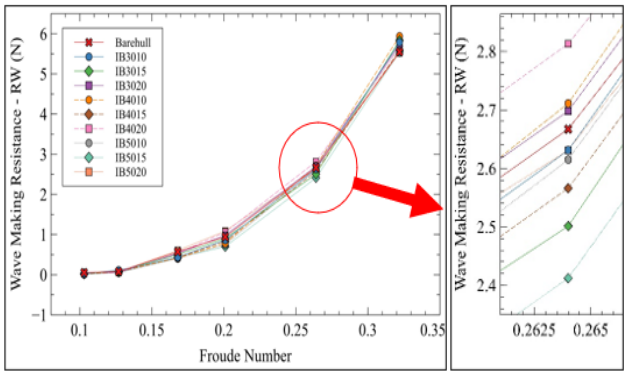

Fig. 16 Inverted bow wave-making resistance (R_W) analysis resul.

Table 11 Wave-making resistance reduction

Model	Fn 0.264	
	R_W (N)	Reduction (%)
Barehull	2.667	-
IB3010	2.631	1.34
IB3015	2.501	6.24
IB3020	2.698	1.17
IB4010	2.711	1.63
IB4015	2.566	3.78
IB4020	2.813	5.49
IB5010	2.615	1.96
IB5015	2.412	9.55
IB5020	2.631	1.35

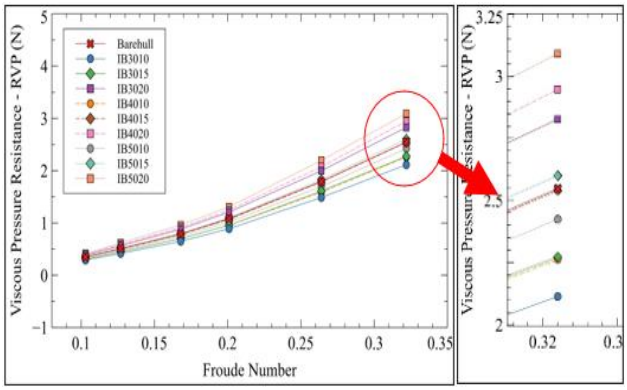

Fig. 17 Inverted bow viscous-pressure resistance (R_{VP}) analysis result

Table 12 Viscous-pressure resistance at Fn 0.322

Model	Fn 0.322	
	R_{VP} (N)	Difference (%)
Barehull	2.547	-
IB3010	2.113	17.06
IB3015	2.273	10.76
IB3020	2.827	10.99
IB4010	2.263	11.16
IB4015	2.540	0.30
IB4020	2.947	15.69
IB5010	2.424	4.85
IB5015	2.600	2.05
IB5020	3.091	21.36

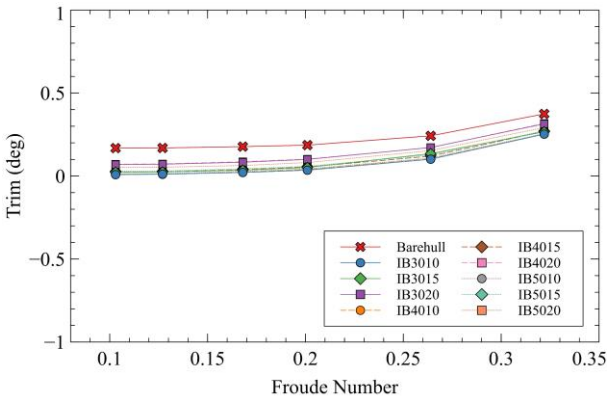

Fig. 18 Inverted bow trim analysis result

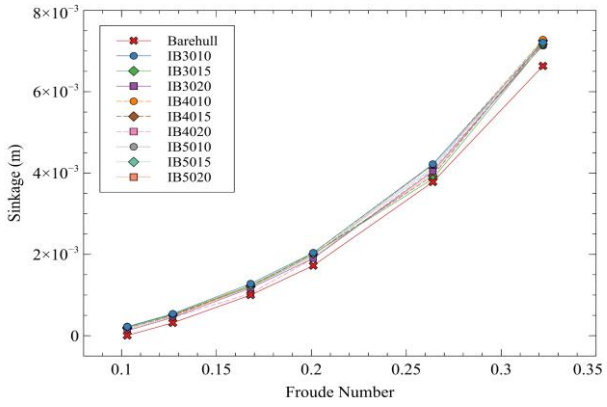

Fig. 19 Inverted bow sinkage analysis result

Figure 18 shows the trim comparison of the inverted bow model. The simulation results found that the trim angle increased with the ship's speed. The results also show that the inverted bow can reduce trim by up to 0.16 degrees. All inverted bow models also have lower trim than barehull models, possibly due to the addition of bow length. As for the sinkage results shown in Fig. 19, it was found that the inverted bow and barehull models did not experience significant changes. The most negligible difference is 4.25 x 10-3 m in IB4020 at Fn 0.168, while the biggest is 6.45 x 10-2 m in IB4010 at Fn 0.322.

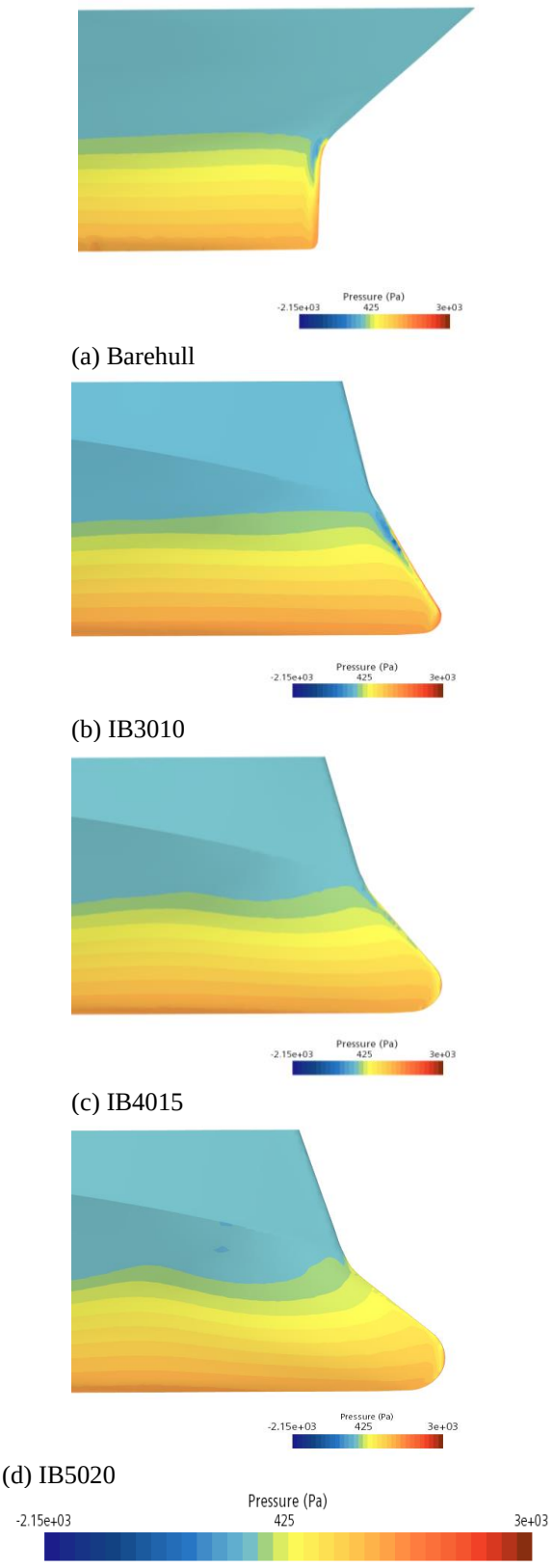

Fig. 20 Pressure distribution in the fore part of the model at Fn = 0.322

The pressure distribution on the hull did not change significantly. The main changes in the bow area, as in Fig. 20, are taken in each model at Fn = 0.322. The observations show that the greater the stem angle and flare bow, the higher the pressure.

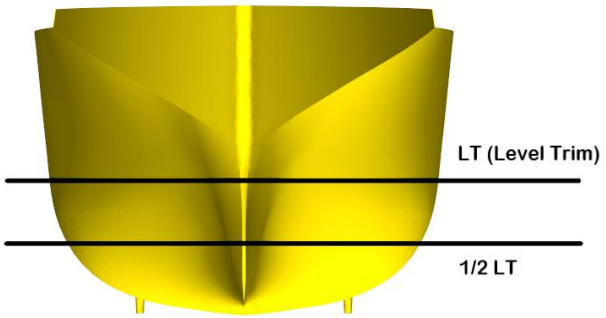

Fig. 21 Location of pressure changes at LT and 1/2 LT

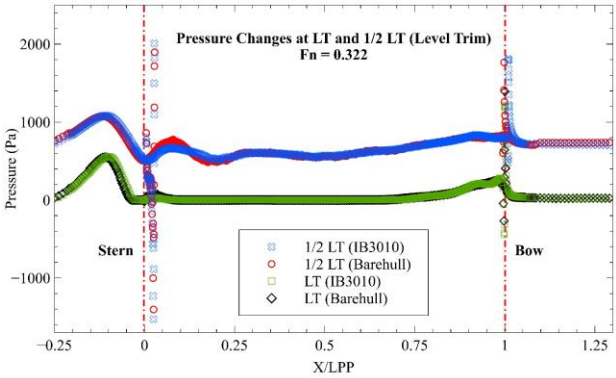

(a) Barehull vs IB3010

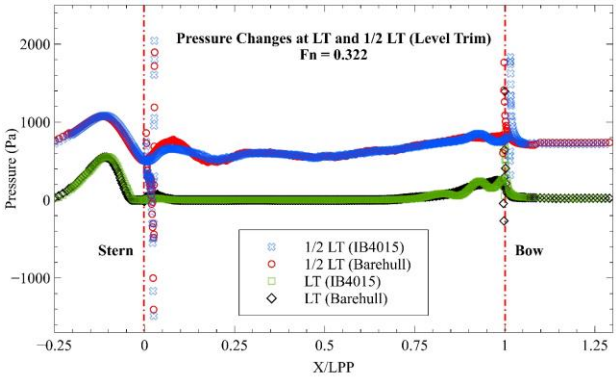

(b) Barehull vs IB4015

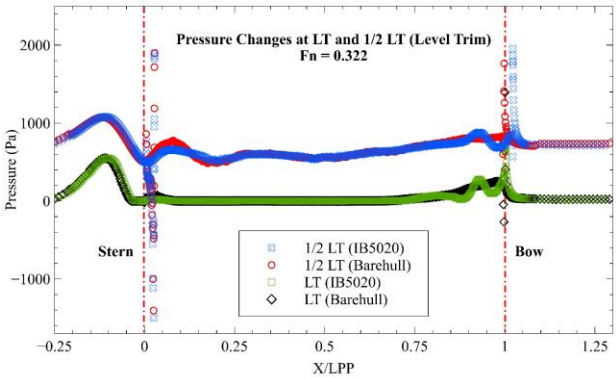

(c) Barehull vs IB5020

Fig. 22 Pressure changes on IB3010, IB4015, and IB5020 at Fn 0.322

Figure 21 shows the location of the pressure changes observation at the trim level location (draft = 0.14m) and 1/2 trim level (draft = 0.07m). Fig. 22 describes the pressure changes along the hull at two observation locations. The results showed increased and decreased pressure on the forebody inverted bow model. In the mid-area, there is no significant change in pressure. As for the aft-body section, there is a pressure drop for the inverted bow model. Furthermore, as shown in Fig. 22, the greater the combination of stem angle and flare bow causes the pressure to change at the forebody area is highest.

Figure 23 illustrates wave cuts taken at three locations Y/B=1, Y/B=2, and Y/B=3 on barehull and IB5015, where the data was taken at Fn 0.264. Figure 24 shows the surface elevation graph on the waterline along hull and center plane. It shows that the surface elevation in the IB5015 bow area is higher than barehull. Figure 25 shows the surface elevation graph at Y/B = 1. In the zoomed image, the IB5015 model produces waves created slightly faster than barehull due to the inverted bow.

Meanwhile, in the area behind the stern, there is a clear difference between the barehull and inverted bow models. The surface elevation of the barehull model is higher than the inverted bow model. This is due to differences in trim on the ship's transom, where the barehull model has a more extensive trim than the inverted bow model, so the water projection in the stern area is higher than in the inverted bow model.

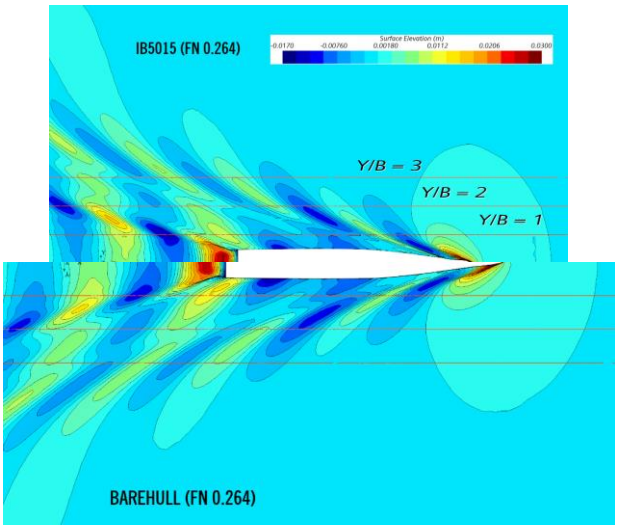

Fig. 23 Locations of the wave cuts

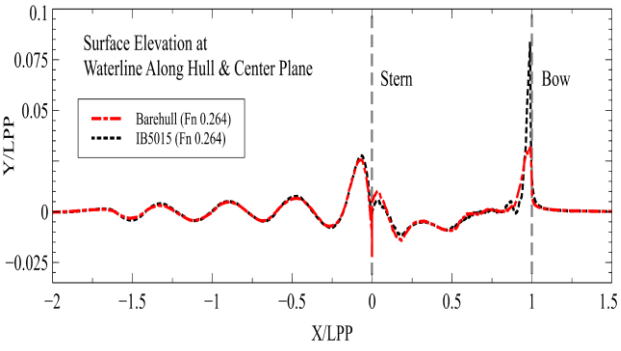

Fig. 24 Surface elevation at waterline along hull and center plane

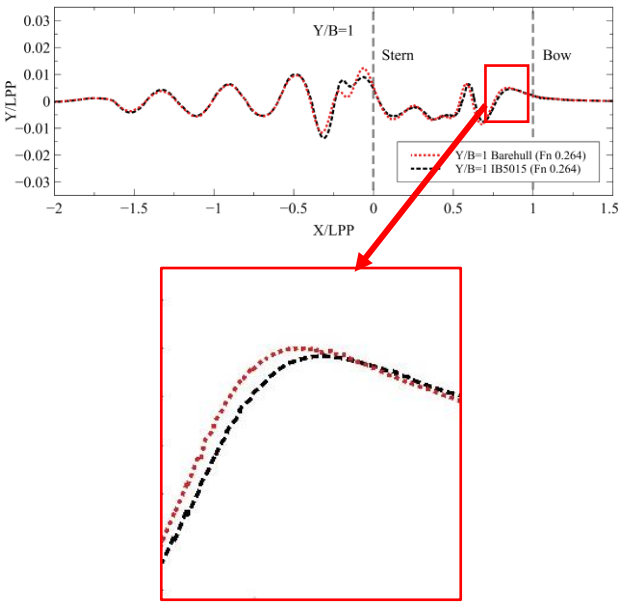

Fig. 25 Wave cuts at Y/B = 1 for barehull and IB5015

4. CONCLUSION

Based on the research that has been done, the validation results of the barehull total resistance show good results. The difference between the experiment and CFD ranges from 0.12% - 2.96%. This demonstrates the highly accurate use of Simcenter Star-CCM+ for simulating ship resistance analysis, proving that the CFD approach is superior to time-consuming experimental tests. Furthermore, the ship's resistance analysis is carried out by dividing it into three components, friction resistance, wave-making resistance, and viscous-pressure resistance.

The results of the analysis indicate that implementing an inverted bow design has a limited impact on friction resistance, with a difference of less than 2.62% observed between the barehull and inverted bow models. However, for wave resistance (RW), the inverted bow design led to a significant reduction. The most notable reduction occurred in IB5015 at Fn 0.264, resulting in a reduction of wave resistance by 9.55%. Additionally, for viscous-pressure resistance (RVP), the highest reduction was observed in IB3010 at Fn 0.322, with a reduction of 17.06%.

Regarding the total resistance (RT), the application of an inverted bow generally resulted in a reduction of total resistance of up to 6.30%. This reduction was most prominent in the case of IB3010 at Fn 0.168. The breakdown of the reduction ratio showed that friction resistance components were reduced by 10.62%, wave resistance by 44.05%, and viscous-pressure resistance by 45.33%. Notably, wave and viscous-pressure resistance played a dominant role in the overall reduction of total resistance. Consequently, the application of an inverted bow design can effectively optimize wave resistance and viscous pressure components, contributing to the enhancement of ship performance.

ACKNOWLEDGEMENTS

We wish to express our sincere gratitude to the Ministry of Education, Culture, Research, and Technology of Indonesia for generously providing funding for this study under grant number 187-06/UN7.6.1/PP/2022. This support has been instrumental in enabling the successful realization of our research efforts.

CONFLICT OF INTEREST

The author(s) declared no potential conflicts of interest with respect to the research, authorship and publication of this article.

AUTHORS CONTRIBUTION

All authors contributed to the conceptualization and Methodology. S. Samuel: project administration, data, funding acquisition. A. Wicaksono, W. A. Kurniawan and E. S. Hadi: draft preparation. T. Tuswan and A. Trimulyono: validation and verification. M. Muryadin: language checking. All authors read and revised the final manuscript.

REFERENCES

Fathuddiin, A., & Samuel, S. (2021). Meshing strategi untuk memprediksi hambatan total pada kapal planing hull. *Rekayasa Mesin*, *12*(2), 381–390. https://doi.org/10.21776/ub.jrm.2021.012.02.15

Firdhaus, A., Suastika, I. K., Kiryanto, K., & Samuel, S. (2021). Benchmark Study of FINETM/Marine CFD Code for the Calculation of Ship Resistance. *Kapal: Jurnal Ilmu Pengetahuan Dan Teknologi Kelautan*, *18*(2), 111–118. http://doi.org/10.14710/kapal.v18i2.39727

Fitriadhy, A., Lim, S. Y., & Maimun, A. (2020). Prediction of an optimum total resistance coefficient on catamaran using design of experiment (DOE) incorporated with CFD approach. *EPI International Journal of Engineering*, *3*(1), 74–83. https://doi.org/10.25042/epi-ije.022020.11

Hoa, N. T. N., Bich, V. N., Tu, T. N., Chien, N. M., & Hien, L. T. (2019). Numerical investigating the effect of water depth on ship resistance using RANS CFD method. *Polish Maritime Research*, *26*(3), 56–64. https://doi.org/10.2478/pomr-2019-0046

IMO. (2020). *Fourth green house gas study 2020.* https://www.imo.org/en/OurWork/Environment/Pages/Fourth-IMO-Greenhouse-Gas-Study-2020.aspx

IMO. (2021). *EEXI and CII - ship carbon intensity and rating system*. https://www.imo.org/en/MediaCentre/HotTopics/Pages/EEXI-CII-FAQ.aspx

ITTC. (2011). *Recommended procedures and guidelines: practical guidelines for ship CFD.* 26th International Towing Tank Conference.

Keuning, J. A., & Walree, F. V. (2006). *The comparison of the hydrodynamic behaviour of three fast patrol boats with special hull geometries.* International Conference on High Performance Marine Vehicles.

Kinaci, O. K., Sukas, O. F., & Bal, S. (2016). Prediction of wave resistance by a Reynolds-averaged Navier-Stokes equation-based computational fluid dynamics approach. *Journal of Engineering for the Maritime Environment, 230*(3), 531–548. https://doi.org/10.1177/1475090215599180

Kiryanto, Hadi, E. S., & Firdhaus, A. (2019). Total resistance analysis on bow form model ulstein X-bow with various angle of flare and stem angle. *IOP Conference Series: Materials Science and Engineering 674*(1), 012003. http://doi.org/10.1088/1757-899X/674/1/012003

Kulkarni, K. H., & Hinge, G. A. (2021a). Performance enhancement in discharge measurement by compound broad crested weir with additive manufacturing. *Larhyss Journal, 48*, 169-188.

Kulkarni, K. H., & Hinge, G. A. (2021b). Comparative study of experimental and CFD analysis for predicting discharge ceofficient of compound broad crested weir. *Water Supply – Water Science and Technology, IWA Publishing, 22*(3), 3283-3296. https://doi.org/10.2166/ws.2021.403

Kulkarni, K. H., & Hinge, G. A. (2023). An energy perpective of composite broad crested weir for measuring accurate discharge. *Larhyss Journal, 54*, 85-106.

Le, T. H., Vu, M. T., Bich, V. N., Phuong, N. K., Ha, N. T. H., Chuan, T. Q., & Tu, T. N. (2021). Numerical investigation on the effect of trim on ship resistance by RANSE method. *Applied Ocean Research, 111*, 102642. https://doi.org/10.1016/j.apor.2021.102642

Lee, J., Park, D. M., & Kim, Y. (2017). Experimental investigation on the added resistance of modified KVLCC2 hull forms with different bow shapes. *Journal of Engineering for the Maritime Environment, 231*(2), 395–410. https://doi.org/10.1177/1475090216643981

Lewis, E. V. (1988). *Principles of naval architecture second revision Vol. II*. Jersey City, NJ: The Society of Naval Architects and Marine Engineers.

Liu, Y., Yu, Z., Zhang, L., Liu, T., Feng, D., & Zhang, J. (2021). A fine drag coefficient model for hull shape of underwater vehicles. *Ocean Engineering, 236*, 109361. https://doi.org/10.1016/j.oceaneng.2021.109361

Liu, Z., Liu, W., Chen, Q., Luo, F., & Zhai, S. (2020). Resistance reduction technology research of high speed ships based on a new type of bow appendage. *Ocean Engineering, 206*, 107246. https://doi.org/10.1016/j.oceaneng.2020.107246

Mohan, N., & Pattamatta, A. (2015). *implementation of two-layer realizable k- ε turbulence model into openfoam for the simulation of nuclear reactor cooling.* International ISHMT-ASTFE Heat and Mass Transfer Conference (IHMTC).

Ozdemir, Y. H., Barlas, B., Yilmaz, T., & Bayraktar, S. (2014). Numerical and experimental study of turbulent free surface flow for a fast ship model. *Brodogradnja, 65*(1), 39–54.

Samuel, S., Iqbal, M., Trimulyono, A., Purwanto, D. B., & Ariani, B. (2022). Evaluasi karakteristik deep-v planing hull dengan menggunakan metode moving grid mesh. *Warta Penelitian Perhubungan, 34*(1), 71–78. http://doi.org/10.25104/warlit.v34i1.1591

Samuel, S., Kim, D. J., Fathuddiin, A., & Zakki, A. F. (2021a). *A numerical ventilation problem on fridsma hull form using an overset grid system.* IOP Conference Series: Materials Science and Engineering *1096*(1), 012041. http://doi.org/10.1088/1757-899X/1096/1/012041

Samuel, S., Trimulyono, A., & Santosa, A. W. B. (2019). Simulasi CFD pada kapal planing hull. *Kapal: Jurnal Ilmu Pengetahuan Dan Teknologi Kelautan, 16*(3), 123–128. https://doi.org/10.14710/kapal.v16i3.26397

Samuel, S., Trimulyono, A., Manik, P., & Chrismianto, D. (2021b). A numerical study of spray strips analysis on fridsma hull form. *Fluids, 6*(11), 420. https://doi.org/10.3390/fluids6110420

Talukdar, B. (2022). Comparative resistance & seakeeping analyses of warship displacement monohulls, when modified to inverted bow forms from conventional bow. *Transactions of the Krylov State Research Centre, 2*(400), 67–78. https://doi.org/10.24937/2542-2324-2022-2-400-67-78

White, J. K., Brizzolara, S., & Beaver, W. (2016). Effect of inverted bow on the hydrodynamic performance of navy combatant hull forms. *Transactions - Society of Naval Architects and Marine Engineers, 123*, 2–13. https://doi.org/10.5957/WMTC-2015-038

Wiliyan, R., Ariana, I. M., & Widhi, D. (2023). *Evaluation of energy efficiency existing ship index (EEXI) on container ship in indonesian shipping.* IOP Conference Series: Earth and Environmental Science *1198*(2023), 012025. https://doi.org/10.1088/1755-1315/1198/1/012025

Yanuar, Gunawan, Sunaryo, & Jamaluddin, A. (2012). Micro-bubble drag reduction on a high speed vessel model. *Journal of Marine Science and Application, 11*(3), 301–304. https://doi.org/10.1007/s11804-012-1136-z